

## Article

# Zirconium Molybdate Nanocomposites' Sensing Platform for the Sensitive and Selective Electrochemical Detection of Adefovir

Wenming Li <sup>1,†</sup>, Jingyun Xiao <sup>1,2,†</sup>, Liangyuan Yao <sup>1,†</sup>, Yanping Wei <sup>1,2</sup>, Jinsong Zuo <sup>1,2</sup>, Weili Zeng <sup>1</sup>, Jianhua Ding <sup>1,\*</sup> and Quanguo He <sup>1,2,3,\*</sup>

<sup>1</sup> Cardiology Department, Zhuzhou People's Hospital, Zhuzhou 421007, China

<sup>2</sup> School of Life Science and Chemistry, Hunan University of Technology, Zhuzhou 412007, China

<sup>3</sup> Hunan Qianjin Xiangjiang Pharmaceutical Joint Stock Co., Ltd., Zhuzhou 412001, China

\* Correspondence: dingjianhua168168@163.com (J.D.); hequanguo@hut.edu.cn (Q.H.);  
Tel./Fax: +86-731-22183426 (Q.H.)

† These authors contributed equally to this work.

**Abstract:** Adefovir (ADV) is an anti-retroviral drug, which can be used to treat acquired immune deficiency syndrome (AIDS) and chronic hepatitis B (CHB), so its quantitative analysis is of great significance. In this work, zirconium molybdate ( $ZrMo_2O_8$ ) was synthesized by a wet chemical method, and a composite with multi-walled carbon nanotubes (MWCNTs) was made.  $ZrMo_2O_8$ -MWCNTs composite was dropped onto the surface of a glassy carbon electrode (GCE) to prepare  $ZrMo_2O_8$ -MWCNTs/GCE, and  $ZrMo_2O_8$ -MWCNTs/GCE was used in the electrochemical detection of ADV for the first time. The preparation method is fast and simple. The materials were characterized by X-ray powder diffraction (XRD), scanning electron microscopy (SEM), energy dispersive spectroscopy (EDS) and cyclic voltammetry (CV). It was electrochemically analysed by differential pulse voltammetry (DPV). Compared with single-material modified electrodes,  $ZrMo_2O_8$ -MWCNTs/GCE showed a vastly improved electrochemical response to ADV. Moreover, the sensor complements the study of the electrochemical detection of ADV. Under optimal conditions, the proposed electrochemical method showed a wide linear range (from 1 to 100  $\mu M$ ) and a low detection limit (0.253  $\mu M$ ). It was successfully tested in serum and urine. In addition, the sensor has the advantages of a simple preparation, fast response, good reproducibility and repeatability. It may be helpful in the potential applications of other substances with similar structures.

**Keywords:** Adefovir; zirconium molybdate; multi-walled carbon nanotubes; electrochemical detection; serum; urine



**Citation:** Li, W.; Xiao, J.; Yao, L.; Wei, Y.; Zuo, J.; Zeng, W.; Ding, J.; He, Q. Zirconium Molybdate Nanocomposites' Sensing Platform for the Sensitive and Selective Electrochemical Detection of Adefovir. *Molecules* **2022**, *27*, 6022. <https://doi.org/10.3390/molecules27186022>

Academic Editor: Seyyed Alireza Mirkhani

Received: 1 September 2022

Accepted: 12 September 2022

Published: 15 September 2022

**Publisher's Note:** MDPI stays neutral with regard to jurisdictional claims in published maps and institutional affiliations.



**Copyright:** © 2022 by the authors. Licensee MDPI, Basel, Switzerland. This article is an open access article distributed under the terms and conditions of the Creative Commons Attribution (CC BY) license (<https://creativecommons.org/licenses/by/4.0/>).

## 1. Introduction

The chemical name of Adefovir (ADV) is 9-(2-phosphonomethoxyethyl)adenine [1]. ADV has shown positive efficacy in the treatment of various viruses, including HIV, herpes viruses and liver viruses, and has a slower rate of development of resistance than Lamivudine, the first oral drug used to treat HBV [2,3]. ADV is relatively safe, and can be used to treat chronic hepatitis B [4]. ADV was approved for marketing by the Food and Drug Administration (FDA) in 2002 and received European Union (EU) marketing authorisation the following year [5]. ADV is the simplest acyclic nucleoside phosphonate (ANP) analogue. One of the reasons for its low oral bioavailability is the limited intestinal permeability of phosphates. However, its oral prodrug, Adefovir dipivoxil, overcomes this, having good oral bioavailability [6]. The antiviral effect of ANP analogues is based on specific interactions between the active diphosphorylated metabolites and viral DNA polymerase [7]. After entering the body, ADV is phosphorylated by cellular kinases to the active metabolite diphosphate, which then competes with the natural substrate deoxyadenosine triphosphate for viral polymerase incorporation. This incorporation leads to

the termination of the viral transcript chain. In order to further understand the intracellular metabolism of Adefovir and other nucleosides and nucleotide analogues, it is necessary to develop a reliable quantitative method [8]. Compared with several other nucleoside analogues, such as Acyclovir and Ganciclovir, ADV bypasses the initial phosphorylation step [9], and is more easily absorbed and utilised by the human body. When ADV is used in long-term treatment, some patients may exhibit drug-related nephrotoxicity [1,10]. Furthermore, it is necessary to study ADV using reliable quantitative methods in clinical metabolic processes. Thus, the quantification of ADV content is essential for people's health.

At present, a series of methods for detecting ADV have been reported, such as liquid chromatography-tandem mass spectrometry [11], liquid chromatography mass spectrometry [12,13], capillary electrophoresis [14], liquid chromatography [15,16], etc. However, these methods are limited by their long analysis time or complex pre-treatment processes, which limits their use in the detection of substances. Electrochemical methods for the determination of additives, small biological molecules and other materials are advantageous, having flexibility, quickness, environmental friendliness and easy operation [17–26]. They also allow for the electrochemical behavior of a given drug to be determined through mechanistic studies, and can even determine the interaction mechanisms between the drug and living cells, and the processes that occur in vivo, after the drug has been taken [27]. At present, square wave voltammetry (SWV) [28] and differential pulse voltammetry (DPV) [29] are used for the electrochemical detection of ADV, which demonstrates that ADV exhibits electrochemical activity. Therefore, it is important to find a more suitable material for modification of the electrodes to improve their electrochemical activity.

Metallic oxide nanomaterials have been used in various ways; for example, tungsten oxide has been explored to detect gases such as  $\text{NH}_3$ ,  $\text{NO}$ ,  $\text{HCHO}$ ,  $\text{O}_2$  and  $\text{H}_2\text{S}$  [30], Pd-loaded  $\text{ZnO}$  has been prepared to detect methane [31], and they have been successfully used as electrode materials [32–39]. Zirconium oxide ( $\text{ZrO}_2$ ) is a kind of metallic oxide nanomaterial used in various applications, such as in electrochemical sensors [40]. However, it has a band gap width of approximately 5.0 eV [41], compared to a band gap of only about 2.57 or 2.74 eV for zirconium molybdate ( $\text{ZrMo}_2\text{O}_8$ ). Therefore,  $\text{ZrMo}_2\text{O}_8$  exhibits excellent photocatalytic properties [42,43]. Bimetallic oxide nanoparticles have received significant attention due to their high specific surface area and excellent selectivity [44]. Molybdate is an eco-friendly inorganic corrosion inhibitor [45], and molybdenum shows remarkable properties in the transfer of electrons to electrodes [46]. At present, erbium molybdate [47], nickel molybdate [48], cerium molybdate [49] and other molybdates have been successfully used for electrochemical detection. It has been shown that bimetallic oxides containing zirconium and molybdenum have advantages in catalysis, ion exchange, and solid conductivity [44]. In addition, soluble acid salts of zirconium ions are widely used as inorganic ion exchange materials [50], chemical sensors [51] and so on, due to their excellent properties.  $\text{ZrMo}_2\text{O}_8$  can not only be used as a negative thermal expansion (NTE) material for  $\text{MX}_2\text{O}_8$ -type compounds ( $\text{M} = \text{Zr}, \text{Ti}, \text{Hf}$  and  $\text{X} = \text{P}, \text{V}, \text{Mo}, \text{W}$ ) [52,53], but also as a catalyst, and in ion exchangers, luminescent materials, humidity sensors, electrochemical sensors, scintillator materials, energy storage devices and photocatalysts [54,55]. These properties and applications mean that  $\text{ZrMo}_2\text{O}_8$  has attracted a great deal of interest.  $\text{ZrMo}_2\text{O}_8$  has several crystal phases: monoclinic phase ( $\beta$ ), trigonal phase ( $\alpha$ ), cubic phase ( $\gamma$ ), orthorhombic phase (LT) and high-pressure phases (monoclinic ( $\delta$ ) and triclinic ( $\epsilon$ )). Their conversion is mainly caused by temperature and pressure [56]. The relatively stable crystal phases, under atmospheric pressure, are the  $\alpha$  and  $\beta$  crystal phases [43].

$\text{ZrMo}_2\text{O}_8$  can be synthesized by co-precipitation, high-pressure-high-temperature synthesis and non-hydrolytic sol-gel methods [57]. The morphology of  $\text{ZrMo}_2\text{O}_8$  has been reported as spherical [55], rod-shaped [58], etc. Lind and Wilkinson [59] used  $\text{Zr}(\text{O}i\text{Pr})_4 \cdot i\text{PrOH}$  as a precursor to form  $\text{ZrMo}_2\text{O}_8$  pristine gels, which were later subjected to heat treatment to obtain  $\alpha$ - $\text{ZrMo}_2\text{O}_8$ ; Shivaneekar and Chudasama [60] used zirconyl chloride octahydrate and ammonium molybdate as raw materials to synthesize  $\text{ZrMo}_2\text{O}_8$  for the catalytic decomposition of hydrogen peroxide; Lind et al. [54] obtained

$\gamma$ -ZrMo<sub>2</sub>O<sub>8</sub> by calcinating zirconium molybdate precursors for the synthesis of cubic-phase zirconium tungstate in the first preparation and characterization of  $\gamma$ -ZrMo<sub>2</sub>O<sub>8</sub>; Lind et al. [58] found that zirconium perchlorate was the most suitable precursor, followed by zirconium nitrate and zirconium chloride, when forming ZrMo<sub>2</sub>O<sub>8</sub> with a rod-shaped structure; Mancheva et al. [56] prepared ZrMo<sub>2</sub>O<sub>8</sub> precursors with ZrOCl<sub>2</sub>·2H<sub>2</sub>O and Na<sub>2</sub>MoO<sub>4</sub>·2H<sub>2</sub>O as raw materials using a co-precipitation method, and systematically investigated the phase transition conditions of ZrMo<sub>2</sub>O<sub>8</sub>.

ZrMo<sub>2</sub>O<sub>8</sub> also shows advantages in electrochemical detection. Nataraj et al. [61] synthesised ZrMo<sub>2</sub>O<sub>8</sub>@rGO using a simple hydrothermal method and prepared the corresponding electrode to detect hydroquinone with differential pulse voltammetry (DPV), which showed favourable results when detecting in river water, wastewater and tap water. The electrode also had excellent anti-interference properties, stability, repeatability and reproducibility. The construction of hydrogen peroxide electrochemical sensors based on spherical ZrMo<sub>2</sub>O<sub>8</sub> nanomaterials was first reported by Kumar et al. [55], and the results showed that the ZrMo<sub>2</sub>O<sub>8</sub> material prepared by a hydrothermal method has a fine crystallinity, regular spherical structure and excellent electrochemical properties. The sensor showed great selectivity even if there were other co-interfering biological substances. Meanwhile, it was shown that ZrMo<sub>2</sub>O<sub>8</sub> is selective to phosphate, having been successfully used to remove phosphate from wastewater [62,63].

Multi-walled carbon nanotubes (MWCNTs) have some excellent properties, such as a high electrical conductivity and high specific surface area. These make them excellent nanomaterials for use in the development of sensor devices [64]. Although MWCNTs have many advantages as carbon materials, they lack selectivity for target molecules when used alone in sensor devices [65]. Therefore, MWCNTs are often combined with other materials to improve their selectivity.

In this work, a simple and fast method was designed based on the idea of compounding, which considers the properties of both ZrMo<sub>2</sub>O<sub>8</sub> and MWCNTs. ZrMo<sub>2</sub>O<sub>8</sub> was synthesized using the wet chemical method and MWCNTs were compounded to form ZrMo<sub>2</sub>O<sub>8</sub>-MWCNTs suspension, and then dropped onto the glassy carbon electrode (GCE) to prepare the modified electrode (ZrMo<sub>2</sub>O<sub>8</sub>-MWCNTs/GCE). The electrochemical properties of ZrMo<sub>2</sub>O<sub>8</sub>-MWCNTs/GCE were investigated by cyclic voltammetry (CV) and differential pulse voltammetry (DPV). The sensor has excellent selectivity, repeatability and reproducibility, and low detection limits. Satisfactory results were obtained when ZrMo<sub>2</sub>O<sub>8</sub>-MWCNTs/GCE was used to determine ADV in biological samples.

## 2. Experimental

### 2.1. Experimental Materials

Adefovir (ADV) was purchased from Bidepharm Technology Co., Ltd. (Shanghai, China) (stored at −20 °C); zirconium oxychloride octahydrate, multi-walled carbon nanotubes (MWCNTs), ammonium molybdate tetrahydrate, *N,N*-dimethylformamide (DMF), sodium acetate trihydrate, potassium ferricyanide, potassium ferrioxalate, potassium chloride and anhydrous ethanol were purchased from Aladdin Biochemical Technology Co., Ltd. (Shanghai, China); glacial acetic acid was purchased from Sinopharm Chemical Reagent Co., Ltd. (Shanghai, China). Other reagents used in the laboratory are analytically pure and were used directly. Serum was provided by the local central hospital (stored at −4 °C) and urine was provided by laboratory staff. The solutions in the experiments were prepared with deionised water (the resistivity being 18.2 M $\Omega$ ).

The preparation method was to weigh 0.0273 g ADV into a 100 mL brown volumetric flask, and then dilute this with deionized water to prepare a 1 mM ADV stock solution, protected from light. A suitable mixture of 1 M acetic acid and 1 M sodium acetate stock solution was used to prepare acetic acid–sodium acetate buffer solution as a support solution for the working solution.

## 2.2. Apparatus

Electrochemical measurements were carried out on a CHI660E electrochemical workstation from Shanghai Chenhua Instruments Co., Ltd. (Shanghai, China). This was achieved using a conventional three-electrode system (with  $\text{ZrMo}_2\text{O}_8$ -MWCNTs/GCE as a working electrode, a platinum wire electrode as a counter-electrode and a saturated calomel electrode (SCE) as a reference electrode). The pH of the solution was determined by a digital PHS-3C pH meter from Shanghai Leici Instrument Factory (Shanghai, China). The morphologies of the nanomaterials were characterized by a German Zeiss Sigma 300 scanning electron microscope. The crystal structures of the nanomaterials were characterized using Bruker nano8 Advanced X-ray powder diffraction.

## 2.3. Preparation of $\text{ZrMo}_2\text{O}_8$ and $\text{ZrMo}_2\text{O}_8$ -MWCNTs Composites

Zirconium oxychloride octahydrate and ammonium molybdate tetrahydrate were weighed to achieve a molar ratio of  $\text{Zr}^{4+}$  to  $\text{Mo}^{6+}$  of 1:2, and then dissolved in deionized water. Zirconium oxychloride octahydrate solution was then slowly added dropwise to the ammonium molybdate solution, with constant stirring, to form a white precipitate. Concentrated hydrochloric acid was added to the precipitate until the white precipitate was completely dissolved. This was aged overnight and refluxed at 100 °C for 12 h, at which point the white precipitate was recreated. The white precipitate was washed by centrifugation with water and ethanol several times and baked at 60 °C for 6 h to obtain the zirconium molybdate precursor ( $\text{ZrMo}_2\text{O}_7(\text{OH})_2 \cdot 2\text{H}_2\text{O}$ ). This was then calcined at 350 °C for 3 h and, after cooling naturally, the temperature was increased to 400 °C for 2 h to obtain  $\text{ZrMo}_2\text{O}_8$  nanoparticles. Subsequently, 1 mg of  $\text{ZrMo}_2\text{O}_8$  was dissolved in 1 mL of DMF to form its corresponding dispersion, and 1 mg of MWCNTs was dissolved in 1 mL of DMF to form its corresponding dispersion. Both were sonicated for 1 h to obtain homogeneous dispersions. Then, the  $\text{ZrMo}_2\text{O}_8$ -MWCNTs composite dispersion was obtained by mixing them with an equal mass ratio.

## 2.4. Fabrication of Modified Electrodes

First, a bare GCE was carefully polished on smooth suede containing 1.0, 0.3 and 0.05  $\mu\text{M}$   $\text{Al}_2\text{O}_3$  powder in sequence, until the electrode surface was smooth. Then, the GCE was alternately washed with anhydrous ethanol and deionized water. Later, the GCE was dried under an infrared light. A certain amount of  $\text{ZrMo}_2\text{O}_8$ -MWCNTs composite dispersion was collected in a pipette gun, dropped onto the surface of GCE and dried under infrared light to obtain  $\text{ZrMo}_2\text{O}_8$ -MWCNTs/GCE. The other electrodes ( $\text{ZrMo}_2\text{O}_8$ /GCE, MWCNTs/GCE) were prepared similarly.

## 2.5. Electrochemical Detection

Electrochemical detection of ADV was carried out by differential pulse voltammetry (DPV) on  $\text{ZrMo}_2\text{O}_8$ -MWCNTs/GCE. A freshly prepared  $\text{ZrMo}_2\text{O}_8$ -MWCNTs/GCE was scanned several times in a blank solution by cyclic voltammetry (CV) to activate the electrode before its first use. The electrode was transferred to a working solution of ADV, diluted with a supporting solution, for detection. After the parameters of each measurement condition were achieved, stirring was stopped and the electrochemical workstation was allowed to rest for a while, before continuing to the next parameter. All electrochemical measurements for this work were carried out at room temperature, and the experimental materials and apparatus used in this work were also at room temperature unless otherwise specified. The preparation process for  $\text{ZrMo}_2\text{O}_8$ -MWCNTs/GCE and its detection of ADV is shown in Figure 1.

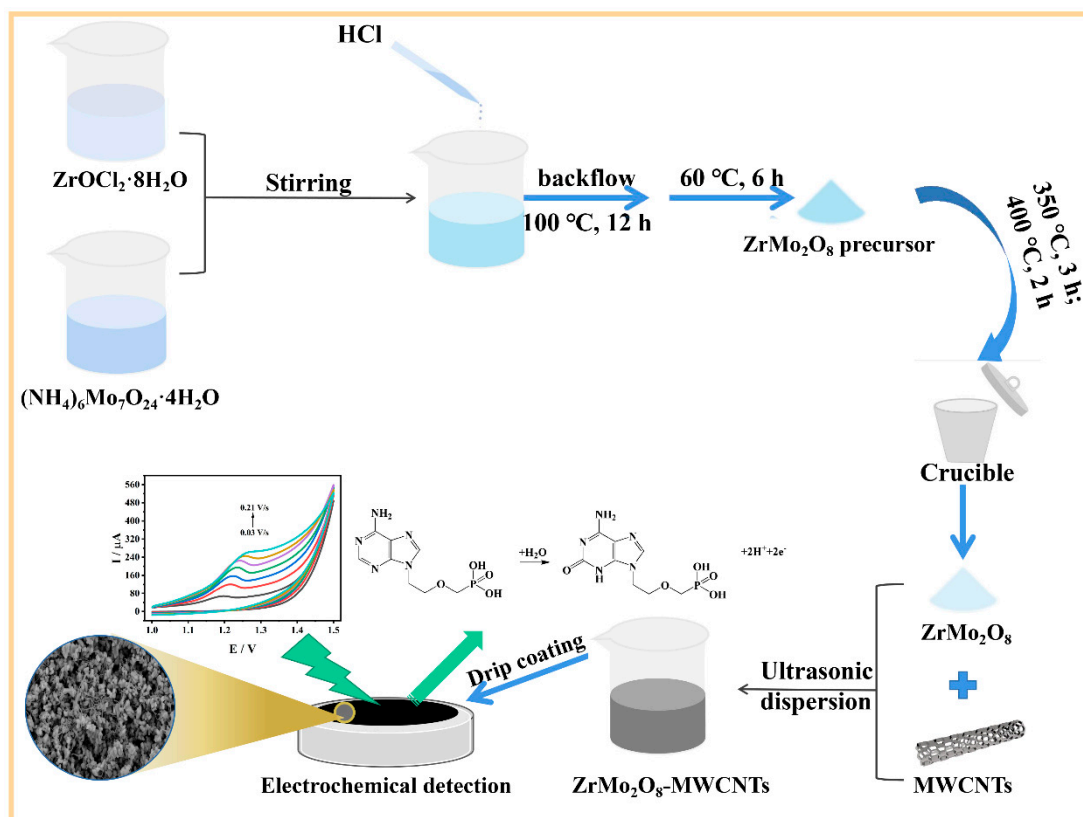


**Figure 1.** Schematic of the preparation process of  $\text{ZrMo}_2\text{O}_8$ -MWCNTs/GCE and its detection of ADV.

### 3. Results and Discussion

#### 3.1. Crystal Phase and Morphology Characterization

The crystal structures of  $\text{ZrMo}_2\text{O}_8$ , MWCNTs and  $\text{ZrMo}_2\text{O}_8$ -MWCNTs composites were investigated by X-ray powder diffractometry (XRD). As shown in Figure 2, diffraction peaks were observed at  $2\theta = 23.14^\circ, 30.44^\circ, 35.32^\circ, 38.61^\circ, 47.38^\circ, 49.99^\circ, 54.16^\circ, 54.27^\circ, 56.59^\circ, 57.36^\circ$  and  $63.35^\circ$ , which correspond to the crystal planes of (112), (004), (114), (303), (215), (305), (315), (216), (306), (332) and (008), respectively. The peak position was consistent with the characteristic diffraction peak of the standard card of  $\text{ZrMo}_2\text{O}_8$  (JCPDS No. 21-1496). The results showed that the synthesized nanomaterial is  $\text{ZrMo}_2\text{O}_8$ . In the XRD spectrum of the  $\text{ZrMo}_2\text{O}_8$ -MWCNTs composite, the typical diffraction peak in MWCNTs also appeared at  $2\theta = 26^\circ$  [66], which was an initial indication that the composite was successfully prepared.

The morphologies of  $\text{ZrMo}_2\text{O}_8$ , MWCNTs and  $\text{ZrMo}_2\text{O}_8$ -MWCNTs composites were characterized by scanning electron microscopy (SEM), as shown in Figure 3. Figure 3A,B show the morphologies of  $\text{ZrMo}_2\text{O}_8$  at different magnification sizes; these were observed to be a rod-like structure, which was consistent with the results reported in the literature that the morphology of the  $\text{ZrMo}_2\text{O}_8$  nanomaterial obtained using zirconium oxychloride octahydrate as a precursor is rod-like [58]. The average size of  $\text{ZrMo}_2\text{O}_8$  was approximately 300–400 nm with relatively uniform particles. In Figure 3C, MWCNTs showed an entangled tubular structure. In Figure 3D, the SEM image of  $\text{ZrMo}_2\text{O}_8$ -MWCNTs shows that tubular MWCNTs were evenly distributed between  $\text{ZrMo}_2\text{O}_8$  nanorods, and had a stable dispersion state. The detection of the target can be achieved by drop coating  $\text{ZrMo}_2\text{O}_8$ -MWCNT composites on the GCE.

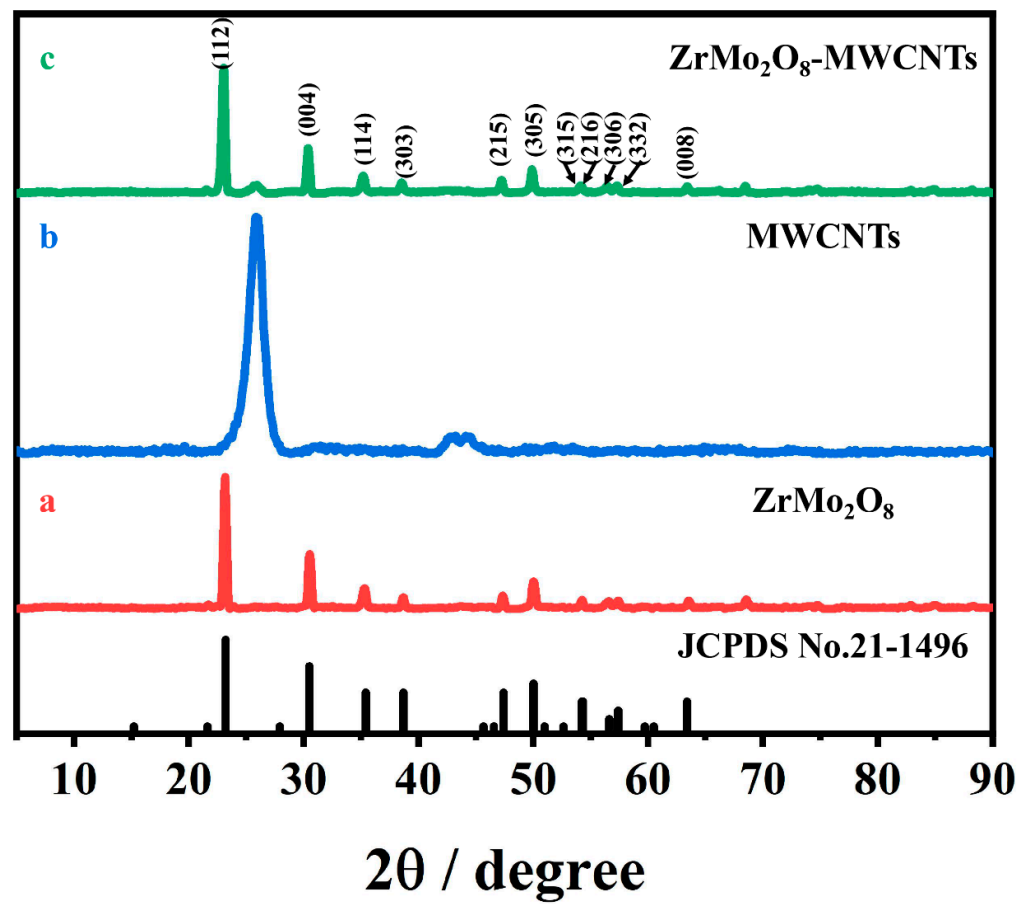


Figure 2. The XRD patterns of ZrMo<sub>2</sub>O<sub>8</sub> (a), MWCNTs (b) and ZrMo<sub>2</sub>O<sub>8</sub>-MWCNTs composites (c).

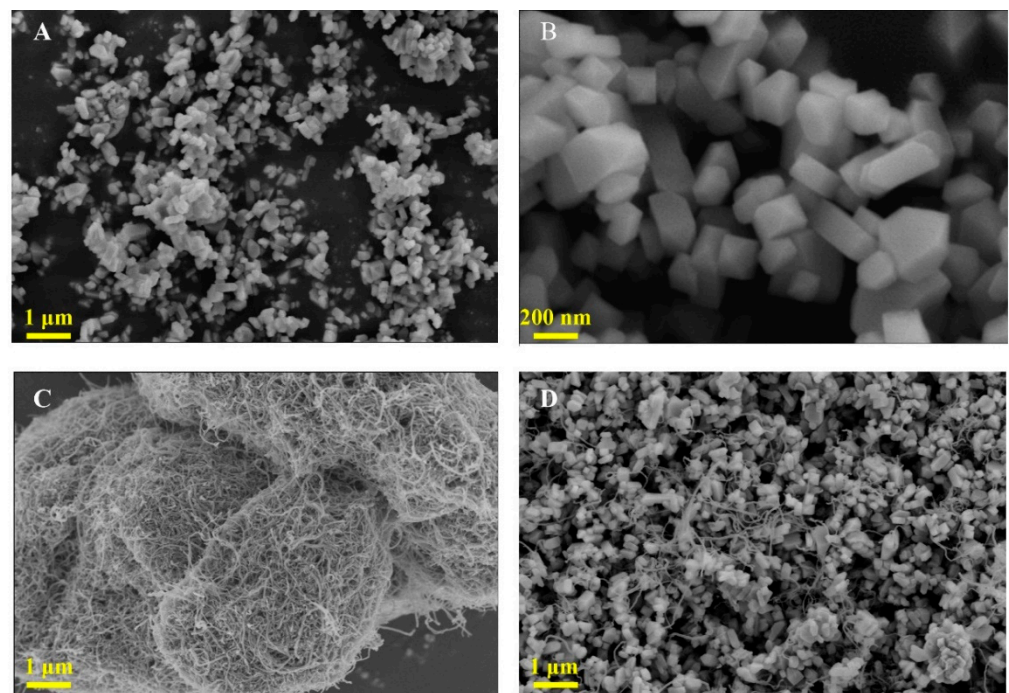
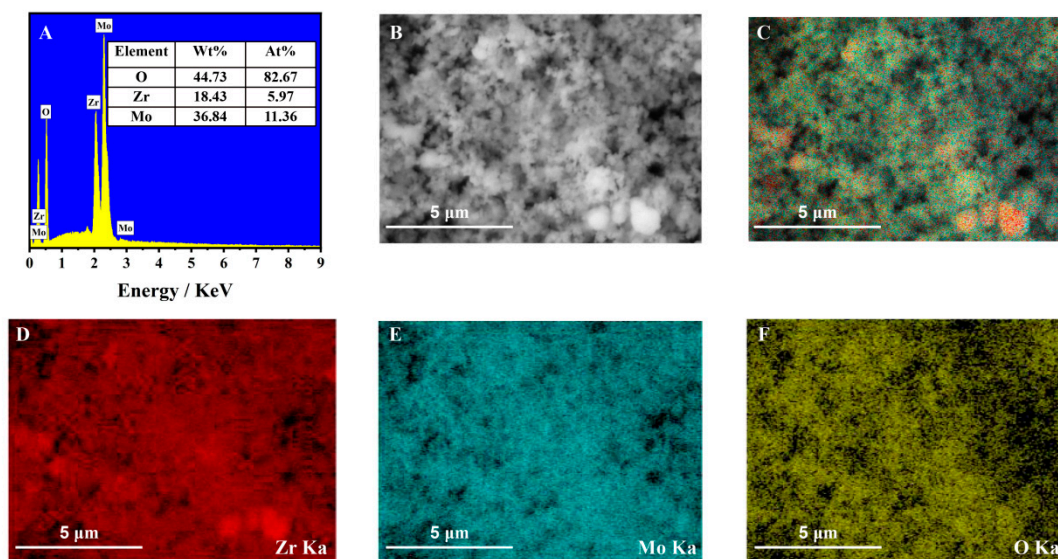


Figure 3. The SEM images of ZrMo<sub>2</sub>O<sub>8</sub> (A,B), MWCNTs (C) and ZrMo<sub>2</sub>O<sub>8</sub>-MWCNTs composites (D).

Figure 4A shows the energy-dispersive spectra (EDS) of the  $\text{ZrMo}_2\text{O}_8$  nanomaterial, in which peaks in oxygen (O), zirconium (Zr) and molybdenum (Mo) can be found. Their contents in the composition were 44.73%, 18.43% and 36.84%, respectively, and their atomic proportions were 82.67%, 5.97% and 11.36%, respectively. The mass ratio and atomic ratio of zirconium and molybdenum to oxygen were compared. The mass ratio of zirconium/oxygen to molybdenum/oxygen in this nanomaterial was approximately 0.5:1, which is larger than the theoretical ratio of 0.47:1 for  $\text{ZrMo}_2\text{O}_8$ . The atomic ratio was approximately 0.51:1, which is larger than the theoretical ratio of 0.5:1 for  $\text{ZrMo}_2\text{O}_8$ . This may be due to the oxygen in the air and some loss of material. The XRD analysis of  $\text{ZrMo}_2\text{O}_8$  further showed that  $\text{ZrMo}_2\text{O}_8$  nanomaterial was successfully prepared. Figure 4D–F shows the individual elemental mappings of the designated area of the  $\text{ZrMo}_2\text{O}_8$  nanomaterial (Figure 4B), and Figure 4C shows its total elemental mapping. It is clear from the distribution of zirconium, molybdenum and oxygen elements in the  $\text{ZrMo}_2\text{O}_8$  nanomaterial, which were found to be uniformly distributed in the nanomaterial, that the  $\text{ZrMo}_2\text{O}_8$  nanomaterial was successfully prepared.



**Figure 4.** The EDS spectrum of  $\text{ZrMo}_2\text{O}_8$  nanomaterial (A); element mappings of all (C) and zirconium, molybdenum and oxygen (D–F) in designated area (B) of  $\text{ZrMo}_2\text{O}_8$  nanomaterial.

### 3.2. Electrochemical Characterisation of Different Electrodes

GCE,  $\text{ZrMo}_2\text{O}_8/\text{GCE}$ , MWCNTs/GCE and  $\text{ZrMo}_2\text{O}_8\text{-MWCNTs}/\text{GCE}$  were immersed in 5 mM  $[\text{Fe}(\text{CN})_6]^{3-/4-}$  and 0.1 M KCl, and electrochemically characterized by CV, at a scan rate of 0.1 V/s, in the potential range of  $-0.2\sim 0.6$  V (Figure 5A). They all show a well-defined pair of quasi-reversible peaks. The currents for the oxidation peak ( $I_{pa}$ ) and reduction peak ( $I_{pc}$ ) on GCE were 111.1  $\mu\text{A}$  and 108.1  $\mu\text{A}$ , respectively, and the corresponding values of potential for oxidation peak ( $E_{pa}$ ) and the reduction peak ( $E_{pc}$ ) were 0.266 V and 0.112 V, respectively. On  $\text{ZrMo}_2\text{O}_8/\text{GCE}$ , the values of  $I_{pa}$  and  $I_{pc}$  were 128.4  $\mu\text{A}$  and 126.1  $\mu\text{A}$ , respectively, and the value of  $\Delta E_p$  ( $\Delta E_p = E_{pa} - E_{pc}$ ) was 0.137 V. The values of these currents were slightly higher than those of GCE, which may be due to the excellent electrical conductivity of  $\text{ZrMo}_2\text{O}_8$ . On MWCNTs/GCE; the values of  $I_{pa}$  and  $I_{pc}$  were 150.1  $\mu\text{A}$  and 151.6  $\mu\text{A}$ , respectively, and the value of  $\Delta E_p$  was 0.111 V. The peak current of MWCNTs/GCE was higher than that of GCE, which may be attributed to the excellent conductivity and catalytic properties of MWCNTs. Compared with the other electrodes,  $\text{ZrMo}_2\text{O}_8\text{-MWCNTs}/\text{GCE}$  had the highest redox peaks. The values of these currents were 162.4  $\mu\text{A}$  and 164.9  $\mu\text{A}$ , respectively and the  $\Delta E_p$  was 0.107 V. This may be due to the synergistic effect of  $\text{ZrMo}_2\text{O}_8$  and MWCNTs, the combination of which improves the sensor

performance. The surface active area of these electrodes was calculated according to the Randles–Sevcik equation [67]:

$$I_p = (2.69 \times 10^5) n^{3/2} D^{1/2} v^{1/2} AC \quad (1)$$

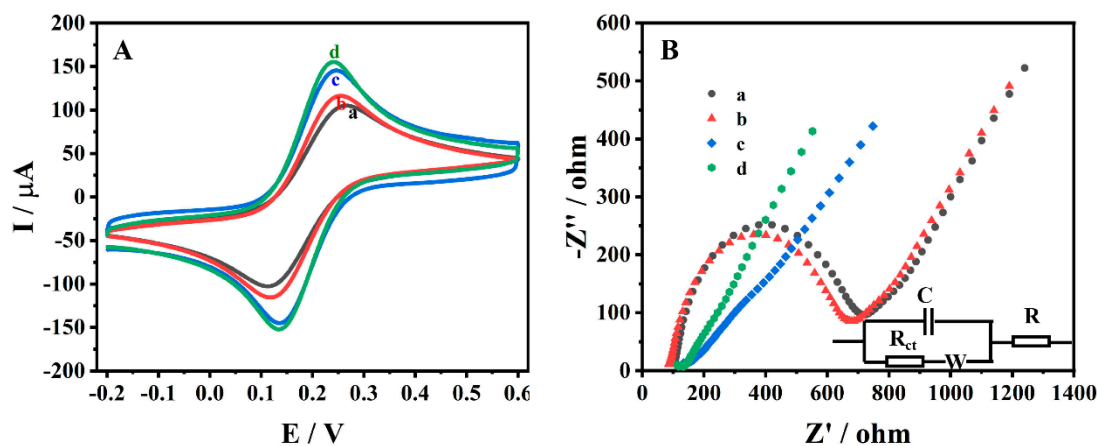


**Figure 5.** CV diagrams (A) and Nyquist plots (B) obtained on different electrodes in a solution of 5 mM  $K_3[Fe(CN)_6]^{3-/4-}$  and 0.1 M KCl (a: GCE, b:  $ZrMo_2O_8$ /GCE, c: MWCNTs/GCE, d:  $ZrMo_2O_8$ -MWCNTs/GCE).

In the above formula,  $I_p$  is the peak current of  $K_3Fe(CN)_6$  (A),  $n$  is the number of transmitted electrons,  $A$  is the effective area ( $cm^2$ ),  $D$  is the diffusion coefficient of  $K_3Fe(CN)_6$  ( $7.6 \times 10^{-6} cm^2 s^{-1}$ ),  $v$  is the scan rate (V/S) and  $C$  is the concentration of  $K_3Fe(CN)_6$  ( $mol/cm^3$ ). The active surface areas for the four GCE,  $ZrMo_2O_8$ /GCE, MWCNTs/GCE and  $ZrMo_2O_8$ -MWCNTs/GCE electrodes were calculated to be  $0.09475 cm^2$ ,  $0.1095 cm^2$ ,  $0.1280 cm^2$  and  $0.1385 cm^2$ , respectively. The results showed that the  $ZrMo_2O_8$ -MWCNTs composites considerably increased the effective active surface area of the electrode, which had better conductivity and more electroactive sites.

Electrochemical impedance spectroscopy (EIS) was used to obtain more information on charge transfer at the electrode/electrolyte interface. Figure 5B shows the Nyquist plots of GCE (a),  $ZrMo_2O_8$ /GCE (b), MWCNTs/GCE (c) and  $ZrMo_2O_8$ -MWCNTs/GCE (d) in 5 mM  $[Fe(CN)_6]^{3-/4-}$  and 0.1 M KCl, which included a semicircle in the high-frequency region and a straight line in the low-frequency region, reflecting the electron transfer properties and diffusion properties. In the Nyquist plot, the charge transfer resistance ( $R_{ct}$ ) is related to the size of the semicircle in the high-frequency region. The Nyquist plots of GCE and  $ZrMo_2O_8$ /GCE showed two distinct semicircles, and the size of the  $ZrMo_2O_8$ /GCE semicircle was smaller than that of the GCE, which is related to the better electrical conductivity of  $ZrMo_2O_8$ . The Nyquist plots of MWCNTs/GCE and  $ZrMo_2O_8$ -MWCNTs/GCE showed almost straight lines for their curves in the high-frequency area, which indicated that their impedances were considerably lower. The  $R_{ct}$  values for GCE,  $ZrMo_2O_8$ /GCE, MWCNTs/GCE and  $ZrMo_2O_8$ -MWCNTs/GCE were  $598.9 \Omega$ ,  $569.4 \Omega$ ,  $17.63 \Omega$  and  $15.9 \Omega$ , respectively. The impedance of  $ZrMo_2O_8$ -MWCNTs/GCE was the lowest, with this result being consistent with the CV characterization results. This indicated that the combination of  $ZrMo_2O_8$  and MWCNTs has a synergistic interaction and is more conducive to the electrochemical reaction.

### 3.3. Electrochemical Behavior of Adefovir on Different Electrodes

The electrochemical performance of GCE (a),  $ZrMo_2O_8$ /GCE (b), MWCNTs/GCE (c) and  $ZrMo_2O_8$ -MWCNTs/GCE (d) in  $1 \times 10^{-4}$  M ADV solution (acetic acid–sodium acetate buffer solution at pH = 5.5) were investigated by DPV, as shown in Figure 6. It can be seen that the peak current of the ADV was the weakest at the GCE ( $I_p = 5.149 \mu A$ ), where

the peak potential was 1.236 V. This was lower than the peak current of  $\text{ZrMo}_2\text{O}_8/\text{GCE}$ , which was found at 1.252 V ( $I_p = 5.758 \mu\text{A}$ ), indicating that  $\text{ZrMo}_2\text{O}_8/\text{GCE}$  improved the electrochemical response of ADV to a certain extent. On the MWCNTs/GCE, the peak oxide current of the ADV was increased to  $21.35 \mu\text{A}$  ( $E_p = 1.168 \text{ V}$ ), which can be attributed to the excellent conductivity of the MWCNTs. In comparison, the  $\text{ZrMo}_2\text{O}_8\text{-MWCNTs}/\text{GCE}$  obtained a maximum peak current at  $E_p = 1.164 \text{ V}$ , where the peak oxide current of the ADV was  $42.57 \mu\text{A}$ , approximately 8 times higher than that of GCE. This indicates that the synergistic interaction of both  $\text{ZrMo}_2\text{O}_8$  and MWCNTs enhanced the electrocatalytic effect, consequently increasing the electrochemical response of ADV.

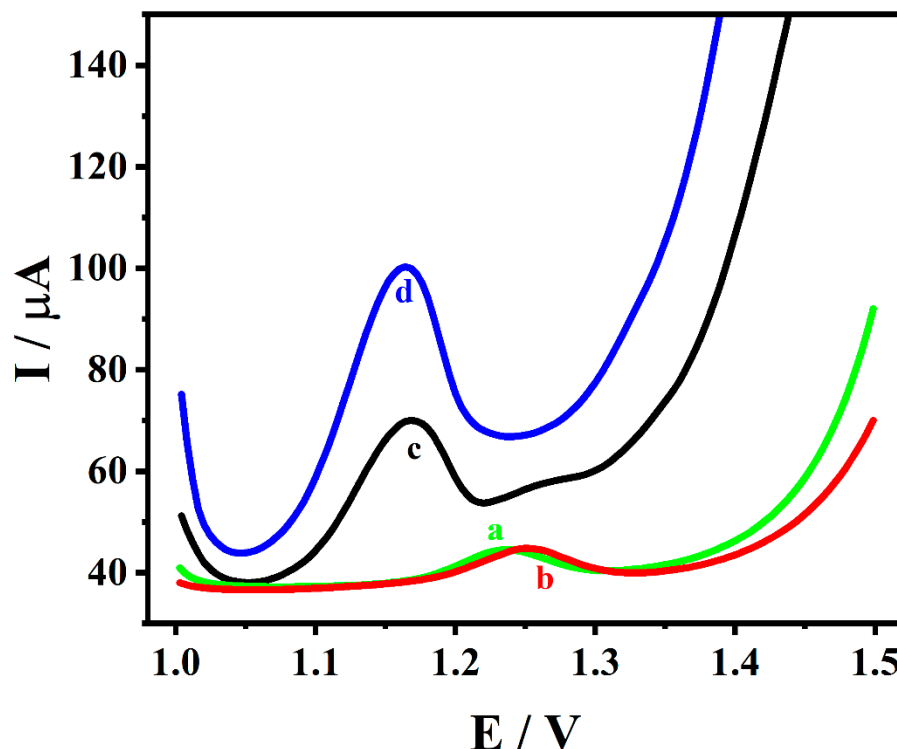


**Figure 6.** DPV diagrams of  $1 \times 10^{-4} \text{ M}$  ADV on different electrodes (a: GCE, b:  $\text{ZrMo}_2\text{O}_8/\text{GCE}$ , c: MWCNTs/GCE, d:  $\text{ZrMo}_2\text{O}_8\text{-MWCNTs}/\text{GCE}$ ).

### 3.4. Effect of Scan Rate

Under the same conditions, the oxidation peak current and peak potential of  $1 \times 10^{-4} \text{ M}$  ADV on  $\text{ZrMo}_2\text{O}_8\text{-MWCNTs}/\text{GCE}$  were detected by CV by changing the scan rate. Figure 7A shows the CV diagram of ADV at a scan rate range of  $0.03\text{--}0.21 \text{ V/s}$ . It can be seen that the reaction of ADV on  $\text{ZrMo}_2\text{O}_8\text{-MWCNTs}/\text{GCE}$  was an irreversible oxidation reaction. As shown in Figure 7B–C, the linear relationship between peak current and  $v$  can be expressed as  $I_p (\mu\text{A}) = 784.3 v (\text{V/s}) + 7.548$  ( $R^2 = 0.9908$ ), indicating that the oxidation reaction of ADV on  $\text{ZrMo}_2\text{O}_8\text{-MWCNTs}/\text{GCE}$  was controlled by adsorption. The linear relationship between peak current and  $v^{1/2}$  can be expressed as  $I_p (\mu\text{A}) = 451.1 v^{1/2} (\text{V/s}) - 52.02$  ( $R^2 = 0.9910$ ), indicating that the oxidation reaction of ADV on  $\text{ZrMo}_2\text{O}_8\text{-MWCNTs}/\text{GCE}$  was controlled by diffusion. Therefore, the oxidation reaction of ADV on  $\text{ZrMo}_2\text{O}_8\text{-MWCNTs}/\text{GCE}$  was controlled by both adsorption and diffusion. Meanwhile, the peak potential of ADV was linearly proportional to  $\ln v$  (Figure 7D) and its linear regression equation can be expressed as  $E_p (\text{V}) = 0.02693 \ln v (\text{V/s}) + 1.293$  ( $R^2 = 0.9806$ ). For completely irreversible electrode processes,  $\alpha$  is usually equal to 0.5 [68]. According to Laviron's equation [68]:

$$E_p = E^0 + (RT/\alpha nF) \ln(RT k^0/\alpha nF) + (RT/\alpha nF) \ln v \quad (2)$$

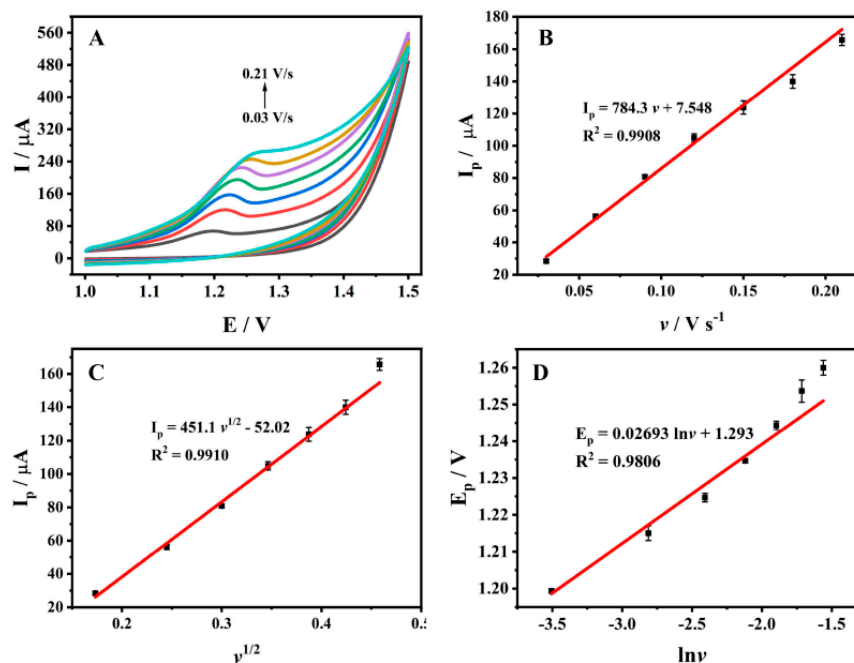


**Figure 7.** (A) CV diagrams of ADV on ZrMo<sub>2</sub>O<sub>8</sub>-MWCNTs/GCE at different scan rates (0.03~0.21 V/s); (B) The plot of the peak current versus  $v$ ; (C) The plot of the peak current versus  $v^{1/2}$ ; (D) The plot of the peak potential versus  $\ln v$ .

In the above formula,  $E_p$  is the peak potential (V);  $E^0$  is the formal potential (V);  $v$  is the scan rate (V/s);  $\alpha$  is the charge transfer coefficient;  $k^0$  is the standard non-homogeneous rate constant;  $n$  is the number of electron transfers;  $T$  is the Kelvin temperature (K);  $F$  is the Faraday constant (96,480 C/mol); and  $R$  is the molar gas constant (8.314 J/(mol·K)). It can be calculated that  $n = 1.907$ , approximately equal to 2, meaning that the electrochemical oxidation of ADV on ZrMo<sub>2</sub>O<sub>8</sub>-MWCNTs/GCE was a two-electron reaction.

### 3.5. Effect of pH

The effect of pH on the acetic acid–sodium acetate buffer solution on the peak current of  $1 \times 10^{-4}$  M ADV on ZrMo<sub>2</sub>O<sub>8</sub>-MWCNTs/GCE was investigated by DPV. Figure 8A shows the DPV diagram for  $1 \times 10^{-4}$  M ADV in a range of pH values (3.5~6.5), indicating that the strength of the current signal and the position of the peak for ADV on ZrMo<sub>2</sub>O<sub>8</sub>-MWCNTs/GCE was significantly influenced by pH. Taking pH = 5.5 as the dividing point, the peak current first increased and then decreased. When the pH value was 5.5, the oxidation peak current of ADV reached a maximum (Figure 8B). Therefore, pH = 5.5 was chosen for electrochemical detection in subsequent experiments. It can be seen from Figure 7C that the oxidation peak potential negatively shifted with the increase in pH value, and the linear relationship between them can be expressed as:  $E_p$  (V) =  $-0.04585$  pH + 1.417 ( $R^2 = 0.9998$ ). According to the Nernst equation [69]:

$$E^\theta = E^0 - (2.303mRT/nF)pH \quad (3)$$

In the above formula,  $m$  and  $n$  are the number of proton transfers and the number of electron transfers, respectively. The equation slope was  $-0.04585$  and, according to the scanning rate, the oxidation of ADV on ZrMo<sub>2</sub>O<sub>8</sub>-MWCNTs/GCE was a two-electron process. Thus, it can be calculated that the value of  $m$  is 1.551, which is approximately equal to 2, indicating that the oxidation of ADV on the ZrMo<sub>2</sub>O<sub>8</sub>-MWCNTs/GCE surface was a two-electron and two-proton reaction. The oxidation mechanism of ADV on ZrMo<sub>2</sub>O<sub>8</sub>-MWCNTs/GCE can be inferred, as shown in Figure 9, which is consistent with the electrochemical oxidation mechanism reported in the literature [29].

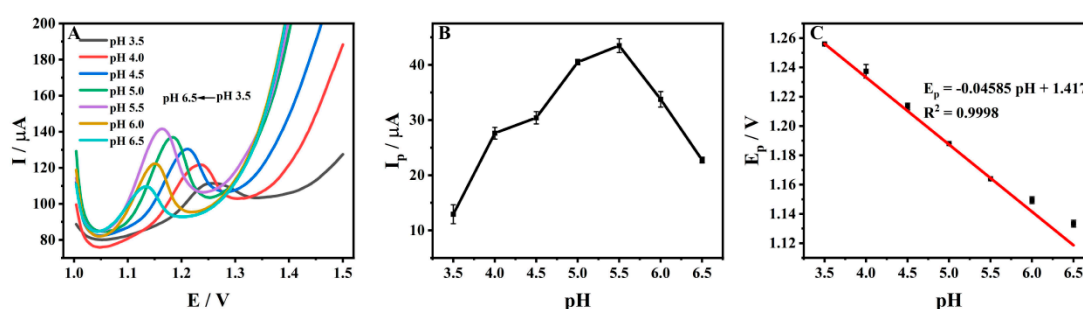


**Figure 8.** DPV diagrams (A), current response (B) and the relationship diagram between peak potential and pH (C) of ADV on ZrMo<sub>2</sub>O<sub>8</sub>-MWCNTs/GCE at different pH values.

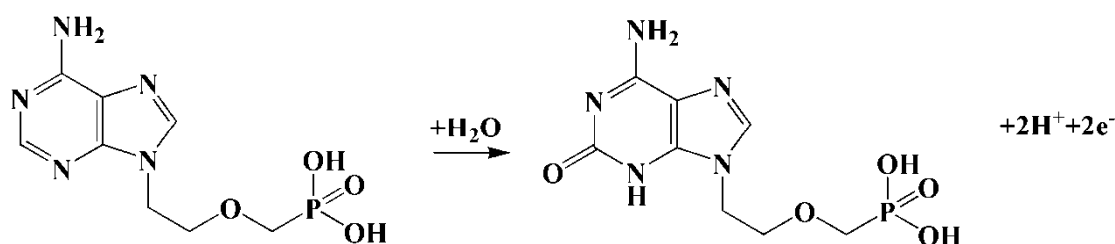


**Figure 9.** The oxidation mechanism of ADV.

### 3.6. Effects of Deposition Conditions and Dropping Amount of ZrMo<sub>2</sub>O<sub>8</sub>-MWCNTs Composites

The effects of deposition potential, deposition time and dropping amount of ZrMo<sub>2</sub>O<sub>8</sub>-MWCNTs composites on the electrochemical activity of  $1 \times 10^{-4}$  M ADV on ZrMo<sub>2</sub>O<sub>8</sub>-MWCNTs/GCE were investigated by DPV. As shown in Figure 10A, when the deposition potential was  $-0.2 \sim 1.0$  V, the degree of ADV adsorption to ZrMo<sub>2</sub>O<sub>8</sub>-MWCNTs/GCE increased. The peak current first increased and then decreased, and reached the maximum at 0 V. At this point, ADV was fully adsorbed. As the deposition potential increased, both the background current and the response current have an effect on the electrochemical detection of the ADV, so 0 V was chosen as the optimal deposition potential. As shown in Figure 10B, the peak current of ADV increased and then decreased with an increasing deposition time of 20~180 s, reaching a maximum at 60 s. This may be due to the fact that the adsorption of ADV on the electrode surface reached supersaturation, resulting in the passivation of ZrMo<sub>2</sub>O<sub>8</sub>-MWCNTs/GCE, which hindered electron transfer and reduced electrode activity. Consequently, 60 s was chosen as the deposition time. The film thickness of the electrode modification material also affects the signal transmission. The effect of different dropping amounts of ZrMo<sub>2</sub>O<sub>8</sub>-MWCNTs composites on the ADV oxidation peak current were investigated in the range of 1~9  $\mu\text{L}$ . As shown in Figure 10C, the peak current increased with the dropping amount in the range of 1~6  $\mu\text{L}$ . When the dropping amount was more than 6  $\mu\text{L}$ , the peak current started to gradually decrease, which may be due to the increase in film thickness hindering electron transfer. For this reason, 6  $\mu\text{L}$  was chosen as the optimal dropping amount. In conclusion, the optimal deposition conditions for the electrochemical detection of ADV on the prepared ZrMo<sub>2</sub>O<sub>8</sub>-MWCNTs/GCE were a deposition potential of 0 V, deposition time of 60 s and dropping amount of 6  $\mu\text{L}$ .

### 3.7. Standard Curve and Detection Limit

The electrochemical detection of ADV at different concentrations (1~100  $\mu\text{M}$ ) was performed by DPV with optimal detection conditions, as shown in Figure 11A. The oxidation peak current of ADV in this range was positively correlated with the magnitude of its concentration (Figure 11B), and the linear regression equation can be expressed as  $I_p (\mu\text{A}) = 0.4507 c (\mu\text{M}) + 1.170$  ( $R^2 = 0.9991$ ). The detection limit was calculated according to the following equation [20]:

$$\text{LOD} = 3s/m \quad (4)$$

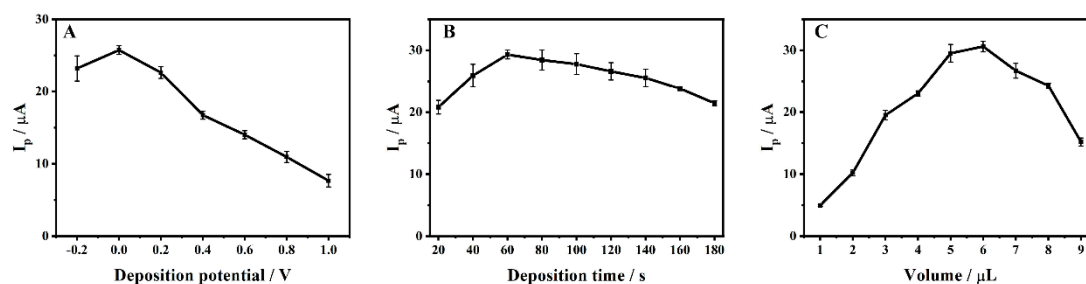


**Figure 10.** Effects of deposition potential (A), deposition time (B) and dropping amount (C) on oxidation peak current of  $1 \times 10^{-4}$  M ADV on ZrMo<sub>2</sub>O<sub>8</sub>-MWCNTs/GCE.

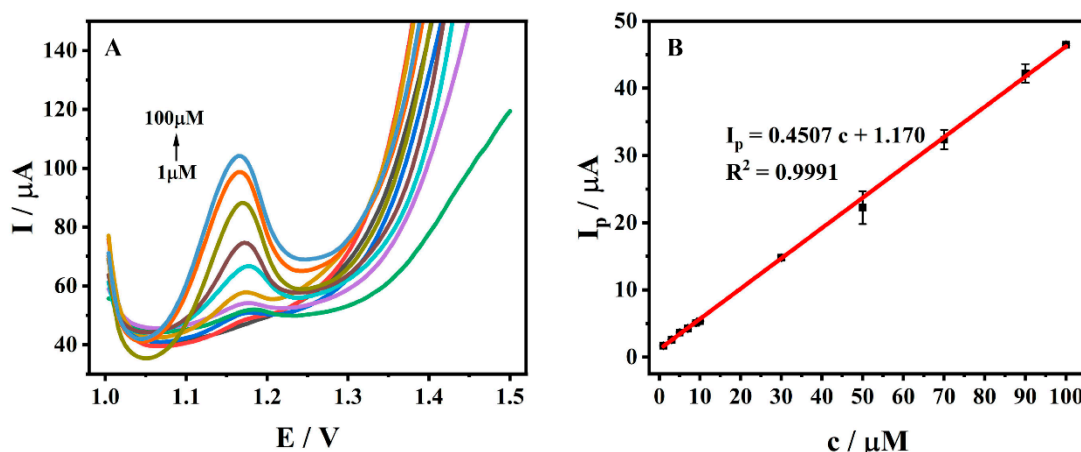


**Figure 11.** (A) DPV diagrams of different concentrations of ADV (1~100  $\mu$ M); (B) The linear relationship between the peak current and ADV concentration in the range of 1~100  $\mu$ M.

In the above formula,  $s$  is the standard deviation of the blank signal ( $n = 5$ ), and  $m$  is the slope of the calibration line within the corresponding range. A detection limit of 0.253  $\mu$ M ( $S/N = 3$ ) was obtained. The prepared ADV electrochemical sensor was compared with other detection methods, with the comparison being given in Table 1. By comparison, ZrMo<sub>2</sub>O<sub>8</sub>-MWCNTs/GCE exhibited a wide linear range (1~100  $\mu$ M) and low detection limit (0.253  $\mu$ M). Meanwhile, compared with the existing electrochemical methods, the ZrMo<sub>2</sub>O<sub>8</sub>-MWCNTs/GCE prepared in this work has a larger linear range for detecting ADV. The detection limit of this method is lower than that of some traditional methods. Therefore, the ZrMo<sub>2</sub>O<sub>8</sub>-MWCNTs/GCE prepared in this work has advantages, and can be used as an alternative method.

**Table 1.** Comparison of different ADV determination methods.

Method	Material	Linear Range ( $\mu$ M)	LOD ( $\mu$ M)	References
capillary electrophoresis	hydroxypropyl methyl cellulose	0.0366~1.83	0.00977	[14]
liquid chromatography	/	0.366~18.3	0.366	[15]
liquid chromatography	/	0.0458~0.586 (Serum)	0.00366 (Serum)	[12]
mass spectrometry	/	0.000183~0.0293 (Urine)	/	[12]
SWV	<sup>a</sup> HMDE	1.830~18.30 (Plasma)	0.6956 (Plasma)	[28]
DPV	HMDE	0.9151~8.236 (drug)	0.2928 (drug)	[28]
DPV	<sup>b</sup> PPY/GCE	0.25~50	0.0031	[29]
DPV	ZrMo <sub>2</sub> O <sub>8</sub> -MWCNTs/GCE	1~100	0.253	this work

<sup>a</sup> HMDE: Hanging mercury drop electrode. <sup>b</sup> PPY/GCE: polypyrrole/glassy carbon electrode.

### 3.8. Investigation of Selectivity

To investigate the selectivity of ZrMo<sub>2</sub>O<sub>8</sub>-MWCNTs/GCE, potential interfering substances that may be present in real situations were added to the  $1 \times 10^{-4}$  M ADV solution under optimal conditions. Three repeated experiments ( $n = 3$ ) were carried out and the average value was taken; the results are shown in Figure 12. Within an allowable relative error of  $\pm 5\%$ , 100-fold inorganic ions (Fe<sup>3+</sup>, Cu<sup>2+</sup>, K<sup>+</sup>, Zn<sup>2+</sup>, Na<sup>+</sup>) did not significantly interfere with the electrochemical response of ADV on ZrMo<sub>2</sub>O<sub>8</sub>-MWCNTs/GCE, and neither did 10-fold organic ions (glucose, L-glutamic acid, dopamine, citric acid, uric acid). The results showed that the prepared ZrMo<sub>2</sub>O<sub>8</sub>-MWCNTs/GCE has excellent selectivity for the analysis of ADV, which makes the detection of ADV in real samples feasible, and can be applied to the detection and analysis of complicated samples.

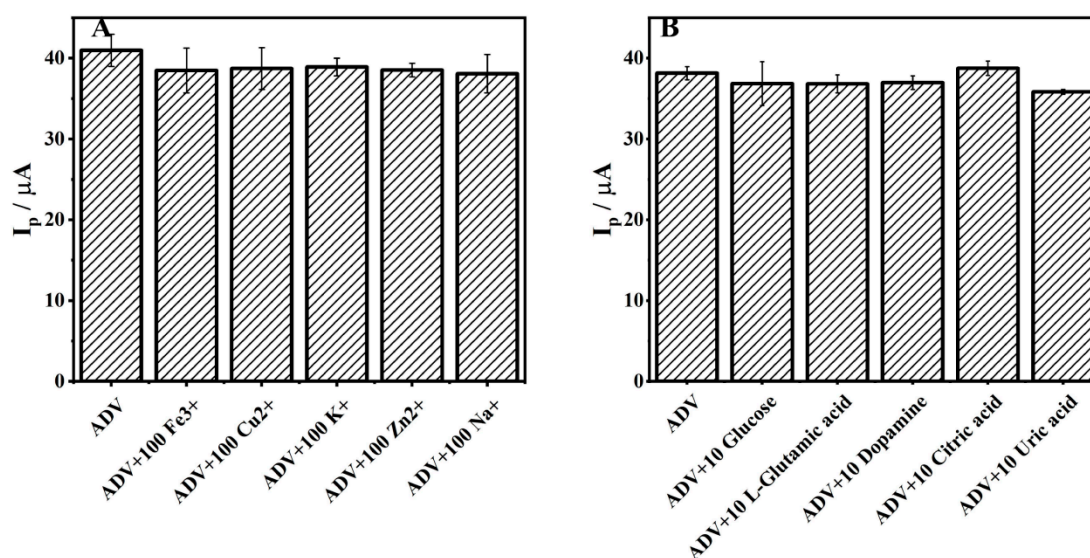


**Figure 12.** Inorganic (A) and organic (B) interference experiments of ADV detected by ZrMo<sub>2</sub>O<sub>8</sub>-MWCNTs/GCE.

### 3.9. Repeatability, Reproducibility and Stability

The repeatability, reproducibility and stability of ZrMo<sub>2</sub>O<sub>8</sub>-MWCNTs/GCE were investigated by DPV in a working solution containing  $1 \times 10^{-4}$  M ADV to provide a basis for the credibility of the test method. On the same ZrMo<sub>2</sub>O<sub>8</sub>-MWCNTs/GCE, the peak current of  $1 \times 10^{-4}$  M ADV in pH 5.5 acetic acid–sodium acetate buffer solution was recorded seven times (Figure 13A) and the relative standard deviation (RSD) of the measured signal was 4.74%, indicating that the sensor has excellent repeatability in the determination of ADV. In addition, five different electrodes were prepared using the same method to investigate the reproducibility of ZrMo<sub>2</sub>O<sub>8</sub>-MWCNTs/GCE. Three repeated experiments ( $n = 3$ ) were carried out and the average value was taken, the results of which are given in Figure 13B. The RSD of the measured signal was 4.88%, indicating that the sensor has an appreciable reproducibility in ADV determination. Two electrodes were prepared, both electrodes were used continuously for five days, and three repeated experiments ( $n = 3$ ) were carried out and the average value was taken. The peak currents of ZrMo<sub>2</sub>O<sub>8</sub>-MWCNTs/GCE were found to be retained at 91.88% and 93.91%, respectively (Figure 13C), indicating that the ZrMo<sub>2</sub>O<sub>8</sub>-MWCNTs/GCE has excellent stability.

### 3.10. Real Sample Detection

To investigate the feasibility of using ZrMo<sub>2</sub>O<sub>8</sub>-MWCNTs/GCE in the determination of ADV in real situations, human serum and urine were used as real samples and tested using method of standard addition and recovery. A total of 1 mL of serum and urine were diluted 100 times, respectively with pH 5.5 acetic acid–sodium acetate buffer solution.

Different concentrations of ADV were added and the real samples were detected by DPV under optimal conditions. The results are given in Table 2, with recoveries ranging from 96.05% to 100.0% for serum and 95.86% to 103.8% for urine. This indicated the feasibility of ZrMo<sub>2</sub>O<sub>8</sub>-MWCNTs/GCE for the detection of ADV in real samples.

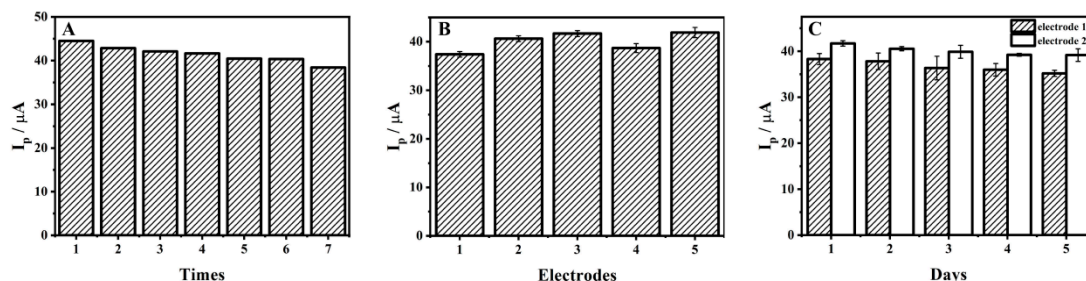


**Figure 13.** Repeatability (A), reproducibility (B) and stability (C) of ZrMo<sub>2</sub>O<sub>8</sub>-MWCNTs/GCE.

**Table 2.** Recovery of ADV in actual samples.

Sample	Measured Value (μM)	Amount Added (μM)	Total Determination (μM)	RSD (%)	Recovery Rate (%)
Serum 1	<sup>a</sup> ND	5	4.908	2.98	98.16
	ND	10	9.996	3.08	99.96
	ND	15	15.00	3.43	100.0
Serum 2	ND	5	4.835	4.83	96.70
	ND	10	9.605	5.03	96.05
	ND	15	14.56	4.36	97.07
Urine 1	ND	5	4.793	5.32	95.86
	ND	10	9.787	1.60	97.87
	ND	15	15.35	1.40	102.3
Urine 2	ND	5	4.884	2.93	97.68
	ND	10	10.38	1.26	103.8
	ND	15	14.87	1.85	99.13

<sup>a</sup> ND = Not detected.

#### 4. Conclusions

In this work, ZrMo<sub>2</sub>O<sub>8</sub> was synthesized using a wet chemistry method with zirconyl chloride octahydrate as a precursor and used as a nanomaterial to investigate a novel electrochemical method for the determination of ADV by ZrMo<sub>2</sub>O<sub>8</sub>-MWCNTs/GCE. The optimal ZrMo<sub>2</sub>O<sub>8</sub>-MWCNTs/GCE conditions for detecting ADV were determined by optimizing the deposition conditions, dropping amount and pH. The prepared ZrMo<sub>2</sub>O<sub>8</sub>-MWCNTs composites were characterized by XRD, SEM and EDS to determine their crystal phase and morphology characteristics. The results show that the ZrMo<sub>2</sub>O<sub>8</sub>-MWCNTs composites exhibited excellent electrochemical activity for ADV under optimal experimental conditions, with a fine linear correlation in the concentration range of 1–100 μM and a detection limit of up to 0.253 μM. In addition, ZrMo<sub>2</sub>O<sub>8</sub>-MWCNTs/GCE showed favourable selectivity, repeatability, reproducibility and stability for ADV, which enabled satisfactory recoveries to be obtained. This allowed it to be used in the determination of ADV in real serum and urine samples, with satisfactory recovery. The electrochemical sensor was simple to prepare and allows for the easy and quick detection of ADV.

**Author Contributions:** Q.H. and J.X. conceived and designed the experiments; J.X., Y.W. and J.Z. performed the experiments; W.L., J.X., L.Y. and J.D. analyzed the data; W.Z., L.Y., J.D. and Q.H. contributed reagents/materials/analysis tools; J.X. and Q.H. wrote the paper. All authors have read and agreed to the published version of the manuscript.

**Funding:** The authors gratefully acknowledge the financial support of the Special Project of 2022 Social Development and Transformation of Scientific and Technological Achievements (No. 51318,

Zhuzhou Municipal Science and Technology Bureau (2020, No. 30 and 2021, No. 44), Doctoral Program Construction of Hunan University of Technology, Postgraduates Innovation Fund of HUT, the NSFC (61703152), Hunan Provincial Natural Science Foundation (2018JJ34) and Project of Science and Technology Department of Hunan Province (2021JJ50035).

**Institutional Review Board Statement:** After the review of the ethics committee of the hospital, the research plan and other materials submitted by this project conform to the medical ethics principles and the requirements of the Helsinki Declaration. The research design has scientific basis, and does not bring unnecessary risks to the subjects. The way to extract the urine, blood and biological fluid of the subjects is standardized, which gives maximum protection to the safety and privacy of the subjects. There is no harm to the environment, and the experiment conforms to the ethical standards of experimental research. Agree to submit papers generated by the project.

**Informed Consent Statement:** Not applicable.

**Data Availability Statement:** Not applicable.

**Conflicts of Interest:** There are no conflict to declare.

### Abbreviations

ADV: Adefovir; AIDS, acquired immune deficiency syndrome; CHB, chronic hepatitis B;  $ZrMo_2O_8$ , zirconium molybdate; MWCNTs, multi-walled carbon nanotubes; GCE, glassy carbon electrode; XRD, X-ray powder diffraction; SEM, scanning electron microscopy; EDS, energy dispersive spectroscopy; CV, cyclic voltammetry; DPV, differential pulse voltammetry; ANP, acyclic nucleoside phosphonate; SWV, square wave voltammetry;  $ZrO_2$ , zirconium oxide; NTE, negative thermal expansion; DMF, *N,N*-dimethylformamide; SCE, saturated calomel electrode; EIS, electrochemical impedance spectroscopy; HMDE, hanging mercury drop electrode; PPy/GCE: polypyrrole/glassy carbon electrode; RSD, relative standard deviation.

### References

1. Mulato, A.S.; Ho, E.S.; Cihlar, T. Nonsteroidal anti-inflammatory drugs efficiently reduce the transport and cytotoxicity of Adefovir mediated by the human renal organic anion transporter 1. *J. Pharmacol. Exp. Ther.* **2000**, *295*, 10–15. [[PubMed](#)]
2. Qi, X.; Xiong, S.; Yang, H.; Miller, M.; Delaney IV, W.E. In vitro susceptibility of Adefovir-associated hepatitis B virus polymerase mutations to other antiviral agents. *Antivir. Ther.* **2007**, *12*, 355–362. [[CrossRef](#)]
3. Lada, O.; Benhamou, Y.; Cahour, A.; Katlama, C.; Poynard, T.; Thibault, V. In vitro susceptibility of Lamivudine-resistant hepatitis B virus to Adefovir and Tenofovir. *Antivir. Ther.* **2004**, *9*, 353–363. [[CrossRef](#)] [[PubMed](#)]
4. Leung, N.; Peng, C.Y.; Hann, H.W.; Sollano, J.; Lao-Tan, J.; Hsu, C.W.; Lesmana, L.; Yuen, M.F.; Jeffers, L.; Sherman, M.; et al. Early hepatitis B virus DNA reduction in hepatitis B e antigen-positive patients with chronic hepatitis B: A randomized international study of Entecavir versus Adefovir. *Hepatology* **2009**, *49*, 72–79. [[CrossRef](#)] [[PubMed](#)]
5. Mehmet, S.S.; Ebru, B.; Serpil, P.; Aylin, D.; Seda, T.; Gonul, A.; Orhan, S.; Engin, A.; Gurol, E.; Enver, U. Detection of hepatitis B virus polymerase gene variants associated with Lamivudine, Adefovir and Entecavir resistance and some undefined mutations isolated from chronic hepatitis B patients in the south of Turkey. *Mol. Genet. Microbiol. Virol.* **2010**, *25*, 178–182. [[CrossRef](#)]
6. Lsanska, L.O.; Ihlar, T.C.; Otruba, I.V.; Oly, A.H. Transport of Adefovir (PMEA) in human T-Lymphoblastoid 9-(2-Phosphonomethoxyethyl) adenine (PMEA; Adefovir) represents the simplest structural type of Acyclic nucleoside phosphonates, an important group of novel antiviral agents. *Compound* **1997**, *62*, 821–828.
7. Naesens, L.; Snoeck, R.; Andrei, G.; Balzarini, J.; Neyts, J.; De Clercq, E. HPMPC (Cidofovir), PMEA (Adefovir) and related acyclic nucleoside phosphonate analogues. A review of their pharmacology and clinical potential in the treatment of viral infections. *Antivir. Chem. Chemother.* **1997**, *8*, 1–23. [[CrossRef](#)]
8. Vela, J.E.; Olson, L.Y.; Huang, A.; Fridland, A.; Ray, A.S. Simultaneous quantitation of the nucleotide analog Adefovir, its phosphorylated anabolites and 2'-deoxyadenosine triphosphate by ion-pairing LC/MS/MS. *J. Chromatogr. B Anal. Technol. Biomed. Life Sci.* **2007**, *848*, 335–343. [[CrossRef](#)]
9. Cundy, K.C. Clinical pharmacokinetics of the antiviral nucleotide analogues Cidofovir and Adefovir. *Clin. Pharmacokinet.* **1999**, *36*, 127–143. [[CrossRef](#)]
10. Ho, E.S.; Lin, D.C.; Mendel, D.B.; Cihlar, T. Cytotoxicity of antiviral nucleotides Adefovir and Cidofovir is induced by the expression of human renal organic anion transporter 1. *J. Am. Soc. Nephrol.* **2000**, *11*, 383–393. [[CrossRef](#)]
11. Goswami, D.; Gurule, S.; Saha, A.; Vats, P.; Khuroo, A.; Monif, T. Liquid chromatography-tandem mass spectrometry method for the estimation of Adefovir in human plasma: Application to a pharmacokinetic study. *J. Pharm. Anal.* **2015**, *5*, 190–199. [[CrossRef](#)] [[PubMed](#)]

12. Sun, D.; Wang, H.; Wang, B.; Guo, R. Development and validation of a sensitive LC-MS/MS method for the determination of Adefovir in human serum and urine. *J. Pharm. Biomed. Anal.* **2006**, *42*, 372–378. [[CrossRef](#)] [[PubMed](#)]
13. Zhang, Y.; Shen, L.; Zhan, Y.; Xiao, Q.Q.; Yang, J. Development and validation of a sensitive LC-MS-MS method for the determination of Adefovir in human serum and urine: Application to a clinical pharmacokinetic study. *J. Chromatogr. Sci.* **2016**, *54*, 507–515. [[CrossRef](#)]
14. Liu, J.; Duan, Y. Field-amplified on-line sample stacking for separation and determination of Adefovir and Tenofovir using capillary electrophoresis. *Asian J. Chem.* **2015**, *27*, 3143–3148. [[CrossRef](#)]
15. Vávrová, K.; Lorencová, K.; Klimentová, J.; Novotný, J.; Hrabálek, A. HPLC method for determination of in vitro delivery through and into porcine skin of Adefovir (PMEA). *J. Chromatogr. B Anal. Technol. Biomed. Life Sci.* **2007**, *853*, 198–203. [[CrossRef](#)]
16. Sparidans, R.W.; Veldkamp, A.; Hoetelmans, R.M.W.; Beijnen, J.H. Improved and simplified liquid chromatographic assay for Adefovir, a novel antiviral drug, in human plasma using derivatization with chloroacetaldehyde. *J. Chromatogr. B Biomed. Sci. Appl.* **1999**, *736*, 115–121. [[CrossRef](#)]
17. Ding, Z.; Deng, P.; Wu, Y.; Tian, Y.; Li, G.; Liu, J.; He, Q. A novel modified electrode for detection of the food colorant sunset yellow based on nanohybrid of MnO<sub>2</sub> nanorods-decorated electrochemically reduced graphene oxide. *Molecules* **2019**, *24*, 1174. [[CrossRef](#)] [[PubMed](#)]
18. He, Q.; Liu, J.; Xia, Y.; Tuo, D.; Deng, P.; Tian, Y.; Wu, Y.; Li, G.; Chen, D. Rapid and sensitive voltammetric detection of Rhodamine B in chili-containing foodstuffs using MnO<sub>2</sub> nanorods/electro-reduced graphene oxide composite. *J. Electrochem. Soc.* **2019**, *166*, B805–B813. [[CrossRef](#)]
19. Tian, Y.; Deng, P.; Wu, Y.; Liu, J.; Li, J.; Li, G.; He, Q. High sensitive voltammetric sensor for nanomolarity vanillin detection in food samples via manganese dioxide nanowires hybridized electrode. *Microchem. J.* **2020**, *157*, 104885. [[CrossRef](#)]
20. Wu, Y.; Deng, P.; Tian, Y.; Feng, J.; Xiao, J.; Li, J.; Liu, J.; Li, G.; He, Q. Simultaneous and sensitive determination of ascorbic acid, dopamine and uric acid via an electrochemical sensor based on PVP-graphene composite. *J. Nanobiotechnol.* **2020**, *18*, 112. [[CrossRef](#)]
21. Zhou, S.; Deng, Z.; Wu, Z.; Xie, M.; Tian, Y.; Wu, Y.; Liu, J.; Li, G.; He, Q. Ta<sub>2</sub>O<sub>5</sub>/rGO nanocomposite modified electrodes for detection of tryptophan through electrochemical route. *Nanomaterials* **2019**, *9*, 811. [[CrossRef](#)]
22. Ning, J.; He, Q.; Luo, X.; Wang, M.; Liu, D.; Wang, J.; Liu, J.; Li, G. Rapid and sensitive determination of vanillin based on a glassy carbon electrode modified with Cu<sub>2</sub>O-electrochemically reduced graphene oxide nanocomposite film. *Sensors* **2018**, *18*, 2762. [[CrossRef](#)]
23. Magesa, F.; Wu, Y.; Tian, Y.; Vianney, J.M.; Buza, J.; He, Q.; Tan, Y. Graphene and graphene like 2D graphitic carbon nitride: Electrochemical detection of food colorants and toxic substances in environment. *Trends Environ. Anal. Chem.* **2019**, *23*, e00064. [[CrossRef](#)]
24. Tian, Y.; Deng, P.; Wu, Y.; Ding, Z.; Li, G.; Liu, J.; He, Q. A simple and efficient molecularly imprinted electrochemical sensor for the selective determination of tryptophan. *Biomolecules* **2019**, *9*, 294. [[CrossRef](#)]
25. He, Q.; Liu, J.; Feng, J.; Wu, Y.; Tian, Y.; Li, G.; Chen, D. Sensitive voltammetric sensor for tryptophan detection by using polyvinylpyrrolidone functionalized graphene/GCE. *Nanomaterials* **2020**, *10*, 125. [[CrossRef](#)]
26. He, Q.; Liu, J.; Liu, X.; Li, G.; Deng, P.; Liang, J.; Chen, D. Sensitive and selective detection of tartrazine based on TiO<sub>2</sub>-electrochemically reduced graphene oxide composite-modified electrodes. *Sensors* **2018**, *18*, 1911. [[CrossRef](#)]
27. Ozkan, S.A.; Uslu, B. From mercury to nanosensors: Past, present and the future perspective of electrochemistry in pharmaceutical and biomedical analysis. *J. Pharm. Biomed. Anal.* **2016**, *130*, 126–140. [[CrossRef](#)]
28. Jain, R.; Sharma, R. Voltammetric quantification of anti-hepatitis drug Adefovir in biological matrix and pharmaceutical formulation. *J. Pharm. Anal.* **2012**, *2*, 98–104. [[CrossRef](#)]
29. Zaabal, M.; Bakirhan, N.K.; Douliche, M.; Kaddour, S.; Saidat, B.; Ozkan, S.A. A new approach on sensitive assay of Adefovir in pharmaceutical and biological fluid samples using polypyrrole modified glassy carbon electrode. *Sens. Actuators B Chem.* **2020**, *323*, 128657. [[CrossRef](#)]
30. Li, J.H.; Wu, J.; Yu, Y.X. DFT exploration of sensor performances of two-dimensional WO<sub>3</sub> to ten small gases in terms of work function and band gap changes and I-V responses. *Appl. Surf. Sci.* **2021**, *546*, 149104. [[CrossRef](#)]
31. Chen, R.; Luo, S.; Xie, D.; Yu, Y.; Xiang, L. Highly dispersive palladium loading on ZnO by galvanic replacements with improved methane sensing performance. *Chemosensors* **2022**, *10*, 329. [[CrossRef](#)]
32. Wang, M.; Chen, K.; Liu, J.; He, Q.; Li, G.; Li, F. Efficiently enhancing electrocatalytic activity of α-MnO<sub>2</sub> nanorods/N-doped ketjenblack carbon for oxygen reduction reaction and oxygen evolution reaction using facile regulated hydrothermal treatment. *Catalysts* **2018**, *8*, 138. [[CrossRef](#)]
33. Chen, K.; Wang, M.; Li, G.; He, Q.; Liu, J.; Li, F. Spherical α-MnO<sub>2</sub> supported on N-KB as efficient electrocatalyst for oxygen reduction in Al-air battery. *Materials* **2018**, *11*, 601. [[CrossRef](#)] [[PubMed](#)]
34. He, Q.; Liu, J.; Liu, X.; Xia, Y.; Li, G.; Deng, P.; Chen, D. Novel electrochemical sensors based on cuprous oxide-electrochemically reduced graphene oxide nanocomposites modified electrode toward sensitive detection of sunset yellow. *Molecules* **2018**, *23*, 2130. [[CrossRef](#)]
35. Wu, Y.; Deng, P.; Tian, Y.; Magesa, F.; Liu, J.; Li, G.; He, Q. Construction of effective electrochemical sensor for the determination of quinoline yellow based on different morphologies of manganese dioxide functionalized graphene. *J. Food Compos. Anal.* **2019**, *84*, 103280. [[CrossRef](#)]

36. Liu, J.; Sun, L.; Li, G.; Hu, J.; He, Q. Ultrasensitive detection of dopamine via electrochemical route on spindle-like  $\alpha$ -Fe<sub>2</sub>O<sub>3</sub> Mesocrystals/rGO modified GCE. *Mater. Res. Bull.* **2021**, *133*, 111050. [[CrossRef](#)]
37. Li, G.; Wu, J.; Jin, H.; Xia, Y.; Liu, J.; He, Q.; Chen, D. Titania/electro-reduced graphene oxide nanohybrid as an efficient electrochemical sensor for the determination of allura red. *Nanomaterials* **2020**, *10*, 307. [[CrossRef](#)]
38. Liu, J.; Dong, S.; He, Q.; Yang, S.; Xie, M.; Deng, P.; Xia, Y.; Li, G. Facile preparation of Fe<sub>3</sub>O<sub>4</sub>/C nanocomposite and its application for cost-effective and sensitive detection of tryptophan. *Biomolecules* **2019**, *9*, 245. [[CrossRef](#)]
39. He, Q.; Tian, Y.; Wu, Y.; Liu, J.; Li, G.; Deng, P.; Chen, D. Electrochemical sensor for rapid and sensitive detection of tryptophan by a Cu<sub>2</sub>O nanoparticles- coated reduced graphene oxide nanocomposite. *Biomolecules* **2019**, *9*, 176. [[CrossRef](#)]
40. Chen, T.W.; Sivasamy Vasantha, A.; Chen, S.M.; Al Farraj, D.A.; Soliman Elshikh, M.; Alkufeidy, R.M.; Al Khulaifi, M.M. Sonochemical synthesis and fabrication of honeycomb like zirconium dioxide with chitosan modified electrode for sensitive electrochemical determination of anti-tuberculosis (TB) drug. *Ultrason. Sonochem.* **2019**, *59*, 104718. [[CrossRef](#)]
41. Pacchioni, G. Role of nanostructuring on the properties of oxide materials: The case of zirconia nanoparticles. *Eur. J. Inorg. Chem.* **2019**, *2019*, 751–761. [[CrossRef](#)]
42. Sahoo, P.P.; Sumithra, S.; Madras, G.; Row, T.G. Synthesis, characterization, and photocatalytic properties of ZrMo<sub>2</sub>O<sub>8</sub>. *J. Phys. Chem. C* **2009**, *113*, 2107–2113. [[CrossRef](#)]
43. Sahoo, P.P.; Sumithra, S.; Madras, G.; Row, G.T.N. Synthesis, structure and photocatalytic properties of  $\beta$ -ZrMo<sub>2</sub>O<sub>8</sub>. *Bull. Mater. Sci.* **2009**, *32*, 337–342. [[CrossRef](#)]
44. Gül, G.Ç.; Kurtuluş, F. Conventional synthesis and characterization of zirconium molybdate, Nd<sub>2</sub>Zr<sub>3</sub>(MoO<sub>4</sub>)<sub>9</sub>. *Int. J. Metall. Mater. Eng.* **2016**, *10*, 1506–1509.
45. Nguyen, T.D.; Nguyen, A.S.; Tran, B.A.; Ke, O.V.; To, T. Molybdate intercalated hydrotalcite/graphene oxide composite as corrosion inhibitor for carbon steel. *Surf. Coat. Technol.* **2020**, *399*, 126165. [[CrossRef](#)]
46. Mohamed, S.N.; Thomas, N.; Tamilmani, J.; Boobalan, T.; Matheswaran, M.; Kalaichelvi, P.; Alagarsamy, A.; Pugazhendhi, A. Bioelectricity generation using iron (II) molybdate nanocatalyst coated anode during treatment of sugar wastewater in microbial fuel cell. *Fuel* **2020**, *277*, 118119. [[CrossRef](#)]
47. Liu, X.; He, J.; Sakthivel, R.; Chung, R. Rare earth erbium molybdate nanoflakes decorated functionalized carbon nanofibers: An affordable and potential catalytic platform for the electrooxidation of phenothiazine. *Electrochim. Acta.* **2020**, *358*, 136885. [[CrossRef](#)]
48. Boopathy, G.; Keerthi, M.; Chen, S.; Umapathy, M.J.; Kumar, B.N. Highly porous nickel molybdate@graphene oxide nanocomposite for the ultrasensitive electrochemical detection of environmental toxic pollutant catechol. *Mater. Chem. Phys.* **2020**, *239*, 121982. [[CrossRef](#)]
49. Karthik, R.; Vinoth Kumar, J.; Chen, S.M.; Karuppiyah, C.; Cheng, Y.H.; Muthuraj, V. A study of electrocatalytic and photocatalytic activity of cerium molybdate nanocubes decorated graphene oxide for the sensing and degradation of antibiotic drug chloramphenicol. *ACS Appl. Mater. Interfaces* **2017**, *9*, 6547–6559. [[CrossRef](#)]
50. Sheha, R.R.; El-Khouly, S.H. Adsorption and diffusion of cesium ions in zirconium(IV) iodomolybdate exchanger. *Chem. Eng. Res. Des.* **2013**, *91*, 942–954. [[CrossRef](#)]
51. Gupta, A.P.; Verma, G.L.; Ikram, S. Studies on a new heteropolyacid-based inorganic ion exchanger; Zirconium(IV) selenomolybdate. *React. Funct. Polym.* **2000**, *43*, 33–41. [[CrossRef](#)]
52. Lind, C.; VanDerveer, D.G.; Wilkinson, A.P.; Chen, J.; Vaughan, M.T.; Weidner, D.J. New high-pressure form of the negative thermal expansion materials zirconium molybdate and hafnium molybdate. *Chem. Mater.* **2001**, *13*, 487–490. [[CrossRef](#)]
53. Krogh Andersen, A.M.; Carlson, S. High-pressure structures of  $\alpha$ - and  $\delta$ -ZrMo<sub>2</sub>O<sub>8</sub>. *Acta Crystallogr. Sect. B.* **2001**, *57*, 20–26. [[CrossRef](#)] [[PubMed](#)]
54. Lind, C.; Wilkinson, A.P.; Hu, Z.; Short, S.; Jorgensen, J.D. Synthesis and properties of the negative thermal expansion material cubic ZrMo<sub>2</sub>O<sub>8</sub>. *Chem. Mater.* **1998**, *10*, 2335–2337. [[CrossRef](#)]
55. Kumar, J.V.; Karthik, R.; Chen, S.M.; Raja, N.; Selvam, V.; Muthuraj, V. Evaluation of a new electrochemical sensor for selective detection of non-enzymatic hydrogen peroxide based on hierarchical nanostructures of zirconium molybdate. *J. Colloid Interface Sci.* **2017**, *500*, 44–53. [[CrossRef](#)] [[PubMed](#)]
56. Mancheva, M.N.; Iordanova, R.S.; Dimitriev, Y.B.; Tyuliev, G.G.; Iliev, T.C. Influence of heat treatment on the phase transition of ZrMo<sub>2</sub>O<sub>8</sub> and photocatalytic activity. *Cent. Eur. J. Chem.* **2011**, *9*, 460–465. [[CrossRef](#)]
57. Iordanova, R.; Mancheva, M.; Dimitriev, Y.; Klissurski, D.; Tyuliev, G.; Kunev, B. Synthesis of ZrMo<sub>2</sub>O<sub>8</sub> polymorphs by a melt quenching method and mechanochemical activation. *J. Alloys Compd.* **2009**, *485*, 104–109. [[CrossRef](#)]
58. Lind, C.; Wilkinson, A.P.; Rawn, C.J.; Payzant, E.A. Preparation of the negative thermal expansion material cubic ZrMo<sub>2</sub>O<sub>8</sub>. *J. Mater. Chem.* **2001**, *11*, 3354–3359. [[CrossRef](#)]
59. Lind, C.; Wilkinson, A.P. Seeding and the non-hydrolytic sol-gel synthesis of ZrW<sub>2</sub>O<sub>8</sub> and ZrMo<sub>2</sub>O<sub>8</sub>. *J. Sol-Gel Sci. Technol.* **2002**, *25*, 51–56. [[CrossRef](#)]
60. Shivaneekar, A.; Chudasama, U. Catalytic behaviour of a Cu(II) complex sorbed on zirconium molybdate in the decomposition of hydrogen peroxide. *Transit. Met. Chem.* **1990**, *15*, 226–230. [[CrossRef](#)]
61. Nataraj, N. An efficient electrochemical sensor based on zirconium molybdate decorated reduced graphene oxide for the detection of Hydroquinone. *Int. J. Electrochem. Sci.* **2020**, *15*, 8321–8335. [[CrossRef](#)]

62. Bui, T.H.; Hong, S.P.; Yoon, J. Enhanced selective removal of arsenic(V) using a hybrid nanoscale zirconium molybdate embedded anion exchange resin. *Environ. Sci. Pollut. Res.* **2019**, *26*, 37046–37053. [[CrossRef](#)]
63. Bui, T.H.; Hong, S.P.; Yoon, J. Development of nanoscale zirconium molybdate embedded anion exchange resin for selective removal of phosphate. *Water Res.* **2018**, *134*, 22–31. [[CrossRef](#)] [[PubMed](#)]
64. Mphuthi, N.G.; Adekunle, A.S.; Ebenso, E.E. Electrocatalytic oxidation of Epinephrine and Norepinephrine at metal oxide doped phthalocyanine/MWCNT composite sensor. *Sci. Rep.* **2016**, *6*, 26938. [[CrossRef](#)] [[PubMed](#)]
65. Naveen, M.H.; Gurudatt, N.G.; Shim, Y. Applications of conducting polymer composites to electrochemical sensors: A review. *Appl. Mater. Today* **2017**, *9*, 419–433. [[CrossRef](#)]
66. Singh, D.K.; Iyer, P.K.; Giri, P.K. Diameter dependence of interwall separation and strain in multiwalled carbon nanotubes probed by X-ray diffraction and Raman scattering studies. *Diam. Relat. Mater.* **2010**, *19*, 1281–1288. [[CrossRef](#)]
67. Feng, J.; Deng, P.; Xiao, J.; Li, J.; Tian, Y.; Wu, Y.; Liu, J.; Li, G.; He, Q. New voltammetric method for determination of tyrosine in foodstuffs using an oxygen-functionalized multi-walled carbon nanotubes modified acetylene black paste electrode. *J. Food Compos. Anal.* **2020**, *96*, 103708. [[CrossRef](#)]
68. Deng, P.; Xiao, J.; Feng, J.; Tian, Y.; Wu, Y.; Li, J.; He, Q. Highly sensitive electrochemical sensor for tyrosine detection using a sub-millimeter electrode. *Microchem. J.* **2021**, *165*, 106106. [[CrossRef](#)]
69. Wei, Y.; Yao, L.; Wu, Y.; Liu, X.; Feng, J.; Ding, J.; Li, K.; He, Q. Ultrasensitive electrochemical detection for nanomolarity Acyclovir at ferrous molybdate nanorods and graphene oxide composited glassy carbon electrode. *Colloids Surf. A Physicochem. Eng. Asp.* **2022**, *641*, 128601. [[CrossRef](#)]